INTERNATIONAL JOURNAL FOR NUMERICAL METHODS IN FLUIDS
*Int. J. Numer. Meth. Fluids* 2010; **63**:185–206
Published online 7 October 2009 in Wiley InterScience (www.interscience.wiley.com). DOI: 10.1002/fld.2182

# A POD goal-oriented error measure for mesh optimization

F. Fang[1,*,†], C. C. Pain[1], I. M. Navon[2], G. J. Gorman[1], M. D. Piggott[1], P. A. Allison[1] and A. J. H. Goddard[1]

[1]*Applied Modelling and Computation Group, Department of Earth Science and Engineering, Imperial College, Prince Consort Road, London SW7 2BP, U.K.*
[2]*Department of Scientific Computing, Florida State University, Tallahassee, FL 32306-4120, U.S.A.*

SUMMARY

The approach for designing an error measure to guide an adaptive meshing algorithm proposed in Power *et al.* (*Ocean Modell.* 2006; **15**:3–38) is extended to use a POD adjoint-based method, thus facilitating efficient primal and adjoint integration in time. The aim is to obtain a new mesh that can adequately resolve all the fields at all time levels, with optimal (w.r.t. the functional) efficiency. The goal-based method solves both the primal and adjoint equations to form the overall error norms, in the form of a metric tensor. The tetrahedral elements are then optimized so that they have unit size in Riemannian space defined with respect to the metric tensor.

This is the first attempt to use POD to estimate an anisotropic error measure. The metric tensor field can be used to direct anisotropic mesh adaptivity. The resulting mesh is optimized to efficiently represent the solution fields over a given time period. The calculation of the error measures is carried out in the reduced space. The POD approach facilitates efficient integration backwards in time and yields the sensitivity analysis necessary for the goal-based error estimates. The accuracy of both the primal and adjoint-reduced models is thus optimized (through the use of anisotropic mesh adaptivity). In addition, the functional for optimizing meshes has been designed to be consistent with that for 4D Var data assimilation.


Received 12 November 2008; Revised 31 July 2009; Accepted 11 August 2009

KEY WORDS: POD; reduced-order models; adjoint; ocean model; finite element; unstructured adaptive mesh; error estimation

,

*Correspondence to: F. Fang, Applied Modelling and Computation Group, Department of Earth Science and Engineering, Imperial College, Prince Consort Road, London SW7 2BP, U.K.
†E-mail: f.fang@imperial.ac.uk, URL: http://amcg.ese.imperial.ac.uk

Contract/grant sponsor: U.K.'s Natural Environment Research Council; contract/grant numbers: NER/A/S/2003/00595, NE/C52101X/1, NE/C51829X/1
Contract/grant sponsor: Engineering and Physical Sciences Research Council; contract/grant number: GR/R60898
Contract/grant sponsor: Leverhulme Trust; contract/grant number: F/07058/AB
Contract/grant sponsor: Imperial College High Performance Computing Service
Contract/grant sponsor: Grantham Institute for Climate Change
Contract/grant sponsor: NSF; contract/grant numbers: ATM-0201808, CCF-0635162

## 1. INTRODUCTION

Simultaneous resolution of a wide range of spatial scales in ocean/atmospheric modelling and diverse CFD problems is clearly desirable. It is often the case that flow in a region of interest is influenced by flow elsewhere at a different scale. When modelling, this issue can be overcome by increasing overall resolution or by separately modelling subregions. Although these approaches can be successful they do incur computational expense. Unstructured and adaptive meshes can potentially avoid these problems as they allow computational effort to resolve important ocean dynamics at diverse scales. The key objective of using adaptive mesh methods is to reduce the overall computational cost in achieving an error goal, thus ensuring that areas of fine resolution are used only when and where they are required.

Mesh adaptivity requires the derivation of an appropriate error measure algorithm. This error measure guides how the mesh is to be adapted. Previous approaches have included: methods developed to measure error with respect to a given energy norm [1–3], interpolation-based methods calculated as an *a priori* measure [4–7] of the error based on both the local mesh size and some high-order derivative of the exact solution, and various types of explicit and implicit *a priori* error measures [8, 9] as well as the implicit equation residual approaches [10–16] in which the same set of equations is solved for the errors, with sources given by the residuals of the governing equations.

An alternate approach for adapting meshes uses an adjoint (or sensitivity)-based error indicator [17–21]. The advantage of this approach is that the error in a functional can be directly related to local residual errors of the primal solution through the adjoint variables. This allows to devise an optimal adaptive mesh for maximizing the accuracy of the functional being chosen [21]. Venditti and Darmofal [21–23] have proposed an anisotropic adaptive procedure for functional outputs of compressible Navier–Stokes simulations for both the finite volume and finite element methods. Balasubramanian [24] has compared the adaptive strategies by Venditti and Darmofal [21–23] and Müller and Giles [25]. Park [26, 27] has further applied the adjoint-based adaptive approach to 3D inviscid and turbulent flows. Formaggia and coworkers [28] have independently developed output-based, anisotropic adaptive procedures for advection–diffusion–reaction and Stokes flows within a finite element framework that also combine adjoint or duality arguments with anisotropic interpolation error estimates.

Power *et al.* [29] has extended the practical utility of the adjoint-based error indicators for adaptive meshes to transient ocean problems. In his work, the adjoint goal-based error indicators have been used to adapt the mesh to optimize specific measures of the dynamics of fluid flow. The goal-based error measure aims to construct a measure of what is deemed important in a problem and design an error measure to optimize the accuracy of this quantity. A limit on the required accuracy for this quantity (goal) can be set and a mesh is optimized to achieve this level of accuracy with minimal computational resources. An adjoint (or sensitivity)-based error measure is formulated that measures the error contribution of each solution variable to an overall goal. The goal is typically embodied in an integral functional, for example, the solution in a small region of the domain of interest. The resulting *a posteriori* error measures involve the solution of both primal and adjoint problems. Mesh adaptivity is achieved with a series of optimization heuristics of the landscape defined by the mesh quality. Mesh quality is gauged with respect to a metric tensor embodying an *a posteriori* error measure, such that an ideal element has sides of unit length when measured with respect to this metric tensor [29]. This results in meshes in which each finite element node has approximately equal (subject to certain boundary conforming constraints and the performance of the mesh optimization heuristics) error contribution to the functional.



DOI: 10.1002/fld

The use of a variable resolution unstructured mesh facilitates the faithful representation of isolated local features and diverse scales. However, the adjoint-based error mesh adaptation involves the solution to primal and adjoint problems. The solution of the adjoint system of equations for realistic problems has proven to be a formidable task [30]. The approach is often hampered in large-scale flow problems by the difficulty of the implementation of the adjoint model, the high computational cost and large memory requirements. This motivates the development of low-order models.

POD provides an efficient method for deriving low-order models of dynamical systems. This technique essentially identifies the most energetic modes in a time-dependent system thus providing a means of obtaining a low-dimensional description of the systems dynamics. To improve the accuracy of reduced models, the goal-oriented approach has been used to optimize the POD bases [31–35]. POD has been used successfully in a wide range of applications [32, 35–49].

The overall objective of this work is to develop an efficient error measure for optimizing meshes that can ensure that areas of fine mesh resolution are used only where they are required over a given time period. In this study, the reduced-order primal and adjoint models using POD are first applied to the error indicator for optimizing meshes. The POD approach facilitates efficient integration backwards in time and delivers the sensitivity analysis necessary for the goal-based error estimates that can be used by mesh adaptivity. By using POD, the computer cost can be significantly reduced while most of kinetic energy can be represented [46]. In addition, it is straightforward to implement the POD-reduced consistent adjoint model. A barotropic wind-driven gyre problem is used to demonstrate the capabilities of the approach developed here.

## 2. PROPER ORTHOGONAL DECOMPOSITION

The model variables $\Psi$ are sampled at defined time intervals (time steps in a discrete model) during the simulation period $[t_1, \ldots, t_K]$, also referred to as snapshots $\Psi = (\Psi_1, \ldots, \Psi_K)^{\mathrm{T}}$ ($K$ being the number of snapshots). The snapshots can be obtained either from a mathematical (numerical) model of the phenomenon or from experiments/observations. The sampled values of variables at the snapshot $k$ are stored in a vector $U_k$ with $\mathcal{N}$ entries ($\mathcal{N}$ being the number of nodes); here, $\Psi$ can represent one of the independent variables $u, v, w, p$. The average of the ensemble of snapshots is defined as:

$$\bar{\Psi}_i = \frac{1}{K} \sum_{k=1}^{K} \Psi_{k,i}, \quad 1 \leqslant i \leqslant \mathcal{N} \tag{1}$$

Taking the deviation from the mean forms

$$V_{k,i} = \Psi_{k,i} - \bar{\Psi}_i, \quad 1 \leqslant i \leqslant \mathcal{N} \tag{2}$$

A collection of all $V_{k,i}$ constructs a rectangular $\mathcal{N}$ by $K$ matrix $A$. The goal of POD is to find a set of orthogonal basis functions $\Phi = \Phi_1, \Phi_2, \ldots, \Phi_K$ such that it maximizes

$$\frac{1}{K} \sum_{k=1}^{K} \sum_{i=1}^{\mathcal{N}} (V_{k,i} \Phi_k) \tag{3}$$



DOI: 10.1002/fld

subject to

$$\sum_{k=1}^{K} \Phi_k^2 = 1 \tag{4}$$

Singular value decomposition (SVD) is used to find the optimal base $\Phi$ of the optimization problem in (3). From SVD, the matrix $A \in R^{\mathcal{N} \times K}$ can be expressed as

$$A = X \begin{pmatrix} \Lambda & 0 \\ 0 & 0 \end{pmatrix} Y^{\mathrm{T}} \tag{5}$$

where $\mathbf{\Lambda} = \mathrm{diag}(\sigma_1, \sigma_2, \ldots, \sigma_d) \in R^{d \times d}$, $X \in R^{\mathcal{N} \times \mathcal{N}}$ and $Y \in R^{K \times K}$ are the matrices that consist of the orthogonal vectors for $AA^{\mathrm{T}}$ and $A^{\mathrm{T}}A$, respectively. The order $\mathcal{N}$ for matrix $AA^{\mathrm{T}}$ is far larger than the order $K$ for matrix $A^{\mathrm{T}}A$. Therefore, a $K \times K$ eigenvalue problem is solved

$$A^{\mathrm{T}} A y_k = \lambda_k y_k, \quad 1 \leqslant k \leqslant K \tag{6}$$

The eigenvalues $\lambda_k$ are real and positive and should be sorted in an descending order. The POD basis vectors $\Phi_k$ associated with the eigenvalues $\lambda_k$ are orthogonal and expressed as follows:

$$\Phi_k = A y_k / \sqrt{\lambda_k} \tag{7}$$

The $k$th eigenvalue is a measure of the kinetic energy transferred within the $k$th basis mode. If the POD spectrum (energy) decays fast enough, practically all the support of the invariant measure is contained in a compact set. Roughly speaking, all the likely realizations in the ensemble can be found in a relatively small set of bounded extent. By neglecting modes corresponding to the small eigenvalues, the following formula is therefore defined to choose a low-dimensional basis of size $M$ ($M \ll K$),

$$I(M) = \frac{\sum_{i=1}^{M} \lambda_i}{\sum_{i=1}^{K} \lambda_i} \tag{8}$$

subject to

$$M = \mathrm{argmin}\{I(M) : I(M) \geqslant \gamma\} \tag{9}$$

where $0 \leqslant \gamma \leqslant 1$ is the percentage of energy that is captured by the POD basis $\Phi_1, \ldots, \Phi_m, \ldots, \Phi_M$.

## 3. AN ADJOINT-BASED SENSITIVITY MEASURE

Power *et al.* [29] developed a goal-based method for defining an anisotropic error metric to guide adaptive meshing. The error contribution to each of the nodal solution variables can be determined and used to substantially improve the accuracy of the functional (a measure of the dynamics of the system, for example vorticity). However, the error metric involves the primal and adjoint solutions and therefore incurs high memory andcomputational costs. In Power's work, the solutions of the



DOI: 10.1002/fld

primal and adjoint models were obtained with a single large time level (the size of a multiple of time steps, equal to the pre-set time between adaptations of the mesh).

In this work, a further step has been made to introduce POD into the primal and adjoint models, thus facilitating efficient integration forwards and backwards in time. This enables one to take into account all nodal primal and adjoint variables at all time levels in the calculation of the metric tensor.

Based on the work [29] two error measures are derived based on the reduced order forward and adjoint solutions, leading to two alternate definitions for the metric tensor. In POD, any variable $\psi$ can be expressed as

$$\psi(t,x,y,z)=\bar{\psi}+\sum_{m=1}^{M}\alpha_{m,\psi}(t)\Phi_{m,\psi}(x,y,z) \tag{10}$$

where $\bar{\psi}$ is the mean of the ensemble of snapshots for the variable $\psi$, $\Phi_{m,\psi}(x,y,z)$ is the POD base for $\psi$, $\alpha_{m,\psi}(t)$ is the corresponding coefficient, $1\leqslant m\leqslant M$ and $M$ is the number of the POD bases.

In this section, the adaptive meshing algorithm developed by Power *et al.* [29] is first outlined. The extension of the algorithm is described in Section 3.2. What distinguishes this work from previous work is: (a) the use of the POD reduced-order modelling and (b) the incorporation of the interpolation error from each time level.

### *3.1. A goal-based error measure*

Suppose a differential equation to be solved is

$$\mathscr{L}\psi_{\text{exact}}-s=0 \tag{11}$$

for source $s$, linear operator $\mathscr{L}$ (the extension to nonlinear operators is relatively straightforward although it can involve considerable algebra) and the exact solution is $\psi_{\text{exact}}\equiv\psi_{\text{exact}}(\mathbf{x},t)$. Taking into account (10), this solution in the reduced space is approximated with a finite element scheme as

$$\psi\equiv\psi(\mathbf{x},t)=\sum_{j=1}^{\mathscr{N}}N_j(\mathbf{x})\Psi_j=\bar{\psi}+\sum_{m=1}^{M}\alpha_{m,\psi}(t)\sum_{j=1}^{\mathscr{N}}N_j(\mathbf{x})\Phi_{m,\psi,j} \tag{12}$$

with $\mathbf{x}=(x,y,z)^{\mathrm{T}}$ being the spatial coordinates, $N_j(\mathbf{x})$ is the finite element basis function associated with node $j$, $\Psi\equiv(\Psi_1,\Psi_2,\ldots,\Psi_{\mathscr{N}})^{\mathrm{T}}$ is the discrete solution vector, $\Phi_{m,\psi,j}$ is the value of the POD bases for the variable $\psi$ at node $j$ and $\mathscr{N}$ is the number of nodes in the finite element mesh.

The aim is to make the equation residual $\mathscr{R}(\psi)\equiv\mathscr{L}\psi-s$ small in some sense. By discretizing (11), the residual vector is then obtained

$$r(\psi)=\mathbf{A}\Psi-S=0 \tag{13}$$

for matrix $\mathbf{A}$ and discretized source $S$. In a practical implementation with inexact arithmetic and possibly the use of iterative solution methods, $r(\psi)$ may not be identically zero. It is assumed to be insignificantly small in this work. This assumption may be relaxed by retaining $r(\psi)$ in the following equations.



DOI: 10.1002/fld

*3.1.1. The functional.* Suppose that the functional whose accuracy is to be optimized is represented as $\Im \equiv \Im(\psi)$, and

$$\Im(\psi) = \int_{\Omega} f(\psi)\, \mathrm{d}\Omega \tag{14}$$

where $\Omega$ is the solution domain. $\Im(\psi)$ may be any derived quantity of the solution $\psi$. Applying a first-order Taylor series expression, the gradient $\partial f/\partial\psi$ near the exact solution $\psi_{\text{exact}}$ can be obtained in discrete form:

$$\left(\frac{\partial \Im}{\partial \Psi}\right)^{\mathrm{T}} (\Psi_{\text{exact}} - \Psi) \approx \Im(\widetilde{\psi}_{\text{exact}}) - \Im(\psi) \tag{15}$$

in which $\Psi_{\text{exact}} \equiv (\Psi_{\text{exact}_1}, \Psi_{\text{exact}_2}, \ldots, \Psi_{\text{exact}_{\mathscr{N}}})^{\mathrm{T}}$ is a vector containing the exact solution at the $\mathscr{N}$ finite element nodes (or control volume cells) and

$$\widetilde{\psi}_{\text{exact}} = \sum_{j=1}^{\mathscr{N}} N_j(\mathbf{x}) \Psi_{\text{exact}_j} \tag{16}$$

That is, $\widetilde{\psi}_{\text{exact}}$ is a finite element (or other numerical) interpolants of the exact solution $\psi_{\text{exact}}$.

*3.1.2. Discrete error measure.* Suppose a nonsingular matrix $\mathbf{A}_{\text{exact}}$ exists such that

$$r_{\text{exact}}(\widetilde{\psi}_{\text{exact}}) = \mathbf{A}_{\text{exact}} \Psi_{\text{exact}} - S = 0 \tag{17}$$

where $\Psi_{\text{exact}}$ is the exact solution at the nodes for a given discretized source vectors $S$. Now define the adjoint solutions $\Psi^*$ and $\Psi^*_{\text{exact}}$ in terms of the adjoint problems

$$\mathbf{A}^{\mathrm{T}} \Psi^* - \frac{\partial \Im}{\partial \Psi} = 0 \tag{18}$$

and

$$\mathbf{A}^{\mathrm{T}}_{\text{exact}} \Psi^*_{\text{exact}} - \frac{\partial \Im}{\partial \Psi} = 0 \tag{19}$$

The adjoint solution in the reduced space is approximated with a finite element scheme as

$$\psi^* \equiv \psi^*(\mathbf{x}, t) = \sum_{j=1}^{\mathscr{N}} N_j(\mathbf{x}) \Psi^*_j = \sum_{m=1}^{M} \alpha^*_{m,\psi}(t) \sum_{j=1}^{\mathscr{N}} N_j(\mathbf{x}) \Phi_{m,\psi,j} \tag{20}$$

where $\Psi^* \equiv (\Psi^*_1, \Psi^*_2, \ldots, \Psi^*_{\mathscr{N}})^{\mathrm{T}}$ is the discrete adjoint solution vector. The corresponding adjoint coefficient $\alpha^*_{m,\psi}(t)$ can be obtained by resolving the adjoint model (18) in the reduced space [46].

Combining (15), (18) and (19), the error measure, in a discrete sense, can be obtained,

$$\Im(\widetilde{\psi}_{\text{exact}}) - \Im(\psi) \approx (\mathbf{A}^{\mathrm{T}} \Psi^*_{\text{exact}})^{\mathrm{T}} (\Psi_{\text{exact}} - \Psi) \tag{21}$$



DOI: 10.1002/fld

### 3.2. Derivation of a metric tensor

In Section 3.1 the error measures were derived. In this section these error measures are modified slightly by approximating the unknown quantities $\mathbf{A}^{\mathrm{T}}\boldsymbol{\Psi}^{*}_{\mathrm{exact}}$ and $r(\widetilde{\psi}_{\mathrm{exact}})$ with known quantities $\widehat{\mathbf{A}^{\mathrm{T}}\boldsymbol{\Psi}^{*}_{\mathrm{exact}}}$ and $\hat{r}(\widetilde{\psi}_{\mathrm{exact}})$, respectively. The error measures equation (21) then becomes

$$\Im(\widetilde{\psi}_{\mathrm{exact}})-\Im(\psi)\approx(\widehat{A^{\mathrm{T}}\boldsymbol{\Psi}^{*}_{\mathrm{exact}}})^{\mathrm{T}}(\boldsymbol{\Psi}_{\mathrm{exact}}-\boldsymbol{\Psi}) \tag{22}$$

The error measure in (22) requires a measure of the error in the primal solution. An alternate error measure that involves a measure of the error in both the primal and adjoint solutions can be expressed as

$$\Im(\widetilde{\psi}_{\mathrm{exact}})-\Im(\psi)\approx\left(\frac{\partial\Im}{\partial\psi}\right)^{\mathrm{T}}(\boldsymbol{\Psi}_{\mathrm{exact}}-\boldsymbol{\Psi})+\hat{r}(\widetilde{\psi}_{\mathrm{exact}})^{\mathrm{T}}(\boldsymbol{\Psi}^{*}_{\mathrm{exact}}-\boldsymbol{\Psi}^{*}) \tag{23}$$

*3.2.1. Defining a metric tensor.* A error metric tensor to guide an adaptive meshing algorithm can be defined as

$$\bar{\mathbf{M}}=\frac{\gamma}{|\varepsilon|}|\mathbf{H}| \tag{24}$$

Here $\mathbf{H}$ is the Hessian matrix, $\varepsilon$ the required level of error and $\gamma$ a scalar constant. The absolute value of the symmetric Hessian matrix is defined as

$$|\mathbf{H}|=\mathbf{V}|\boldsymbol{\Lambda}|\mathbf{V}^{\mathrm{T}} \tag{25}$$

where the matrices $\mathbf{V}$ and $\boldsymbol{\Lambda}$ contain the eigenvectors $\mathbf{e}_i$ and eigenvalues $\Lambda_i$ of the Hessian matrix $\mathbf{H}$, respectively. Ideal elements then have sides of length unity when measured with respect to the metric tensor. The discrete (nodal) form of $\varepsilon$, from (22), is

$$\varepsilon_i=\frac{\widetilde{\delta\Im}}{\sum_{n=1}^{\mathrm{NT}}|(\widehat{\mathbf{A}^{\mathrm{T}}\boldsymbol{\Psi}^{*}_{\mathrm{exact}}})^{n}_{i}|} \tag{26}$$

Here $n$ is the time index, NT is the number of time levels, $(\widehat{\mathbf{A}^{\mathrm{T}}\boldsymbol{\Psi}^{*}_{\mathrm{exact}}})^{n}_{i}$ is the $i$th entry of the vector $(\widehat{\mathbf{A}^{\mathrm{T}}\boldsymbol{\Psi}^{*}_{\mathrm{exact}}})^{n}$. Suppose $\delta\Im$ is the acceptable error in $\Im$; then assuming the error contribution to $\Im$ is the same for each node, then define

$$\widetilde{\delta\Im}=\frac{\delta\Im}{\mathscr{N}} \tag{27}$$

*3.2.2. Application to multiple field problems.* For each solution variable $l$ (here, a variable is one of the various variables $u, v, w, p$ at a single time step $n$ or at any other time step, that is, both $u^n$ and $u^{n+1}$ can be considered separate variables) at each node $i$, it is possible to define two Hessians: $\mathbf{H}^{l,n}_{i}$ associated with the primal solution $\psi^{l,n}_{i}$ and $\mathbf{H}^{*l,n}_{i}$ associated with the adjoint solution $\psi^{*l,n}_{i}$. The Hessian matrices are defined as

$$\mathbf{H}^{l,n}_{i}\equiv(\nabla^{\mathrm{T}}\nabla\psi^{l,n})_i,\quad \mathbf{H}^{*l,n}_{i}\equiv(\nabla^{\mathrm{T}}\nabla\psi^{*l,n})_i \tag{28}$$



DOI: 10.1002/fld

where $\psi^{l,n}$ and $\psi^{*l,n}$ can be calculated by

$$\psi^{l,n} \equiv \psi^{l,n}(\mathbf{x},t) = \sum_{j=1}^{\mathscr{N}} N_j(\mathbf{x})\Psi_j^{l,n} = \bar{\psi}^l(\mathbf{x}) + \sum_{m=1}^{M^l} \alpha_{m,\psi}^{l,n} \sum_{j=1}^{\mathscr{N}} N_j \Phi_{m,\psi,j}^l \tag{29}$$

$$\psi^{*l,n} \equiv \psi^{*l,n}(\mathbf{x},t) = \sum_{j=1}^{\mathscr{N}} N_j(\mathbf{x})\Psi^{*l,n}_j = \sum_{m=1}^{M^l} \alpha^{*l,n}_{m,\psi} \sum_{j=1}^{\mathscr{N}} N_j \Phi^l_{m,\psi,j} \tag{30}$$

where $1 \leqslant m \leqslant M^l$, $\Phi_{m,\psi,j}^{l,n}$ is the POD bases for $\psi_j^{l,n}$ at node $j$, $\alpha_{m,\psi}^{l,n}$ and $\alpha^{*l,n}_{m,\psi}$ are the corresponding coefficients obtained from the primal and adjoint-reduced order models, respectively, and $M^l$ is the number of the POD bases. To calculate the Hessians, the method presented in [50] is followed. Galerkin projections are repeatedly applied to calculate the first derivatives [29].

If there are $\mathscr{M}$ solution variables per node, then an averaged Hessian $\bar{\mathbf{H}}_i$ associated with node $i$ can be defined as

$$\bar{\mathbf{H}}_i = \frac{1}{\sum_{n=1}^{\mathrm{NT}} \sum_{l=1}^{\mathscr{M}} |\lambda_i^{l,n}|} \sum_{n=1}^{\mathrm{NT}} \sum_{l=1}^{\mathscr{M}} |\lambda_i^{l,n}| |\mathbf{H}_i^{l,n}| \tag{31}$$

where

$$\lambda_i^{l,n} = (\widehat{\mathbf{A}^{\mathrm{T}}\Psi^*_{\mathrm{exact}}})_i^{l,n} \tag{32}$$

$(\widehat{\mathbf{A}^{\mathrm{T}}\Psi^*_{\mathrm{exact}}})_i^{l,n}$ at node $i$ can be approximately obtained by

$$|(\widehat{\mathbf{A}^{\mathrm{T}}\Psi^*_{\mathrm{exact}}})_i^{l,n}| = \left| \left( \sum_{j \neq i} A_{i,j}^{\mathrm{T}} \Psi_j^* + A_{i,i}^{\mathrm{T}} \bar{\Psi}_i^* - \frac{\partial \Im}{\partial \Psi} \right)^{l,n} \right| \tag{33}$$

where $\bar{\Psi}_i^*$ is the average adjoint value of $\Psi^*$ around node $i$. Absolute values of the Hessian matrices $|\mathbf{H}_i^{i,n}|$ are as given by (25). This technique uses (22) as the basis for this average. Using the error measure defined by (22), the metric tensor field can be found. An interpolation error $\bar{\varepsilon}_i$ at node $i$ can be defined as

$$\bar{\varepsilon}_i = \frac{\widetilde{\delta\Im}}{\sum_{n=1}^{\mathrm{NT}} \sum_{l=1}^{\mathscr{M}} |\lambda_i^{l,n}|} \tag{34}$$

Then the nodal metric tensor $\bar{\mathbf{M}}_i$ is obtained from

$$\bar{\mathbf{M}}_i = \frac{\gamma}{|\bar{\varepsilon}_i|} |\bar{\mathbf{H}}_i| \tag{35}$$

Using the adjoint error measure defined by (23), a second metric tensor can be obtained based on the primal and adjoint solutions. To that end, suppose that

$$\lambda^{*l,n}_i = \hat{r}(\psi)_i^{l,n} \tag{36}$$



DOI: 10.1002/fld

and the residual at node $i$ can be approximately obtained by

$$|\hat{r}_i^{l,n}| = \left| \left( \sum_{j \neq i} A_{i,j} \Psi_j + A_{i,i} \bar{\Psi}_i - s_i \right)^{l,n} \right| \tag{37}$$

where $\bar{\Psi}_i$ is the average value of $\Psi$ around node $i$. It may be valuable to consider a modified adjoint metric tensor constructed in a similar manner to that used in (31). Taking this into consideration, a modified averaged adjoint Hessian, $\bar{\mathbf{H}}_i^*$ say, can be defined as

$$\bar{\mathbf{H}}_i^* = \frac{1}{\sum_{n=1}^{\mathrm{NT}} \sum_{l=1}^{\mathscr{M}} |\lambda^{*l,n}_i|} \sum_{n=1}^{\mathrm{NT}} \sum_{l=1}^{\mathscr{M}} |\lambda^{*l,n}_i| |\mathbf{H}^{*l,n}_i| \tag{38}$$

Consequently a modified adjoint-based interpolation error $\bar{\varepsilon}_i^*$ can be defined as:

$$\bar{\varepsilon}_i^* = \frac{\widetilde{\delta \Im}}{\sum_{n=1}^{\mathrm{NT}} \sum_{l=1}^{\mathscr{M}} |\lambda^{*l,n}_i|} \tag{39}$$

So a modified adjoint-based metric tensor $\bar{\mathbf{M}}_i^*$ for node $i$ is obtained from

$$\bar{\mathbf{M}}_i^* = \frac{\gamma}{|\bar{\varepsilon}_i^*|} |\bar{\mathbf{H}}_i^*| \tag{40}$$

The matrix tensors $\bar{\mathbf{M}}^*$ and $\bar{\mathbf{M}}$ are designed to result in conservatively small element length scales. Thus, the minimal ellipsoid that superscribes both ellipses is an appropriate metric for use with mesh adaptivity (see Figure 1). Importantly this new metric retains the anisotropic information of both the matrices $\bar{\mathbf{M}}^*$ and $\bar{\mathbf{M}}$.

$$\bar{\bar{\mathbf{M}}}_i^{\mathscr{G}_s} = \mathscr{G}_s(\bar{\mathbf{M}}_i, \bar{\mathbf{M}}_i^*) \tag{41}$$

The operator $\mathscr{G}_s$ is used to superscribe the matrix tensors $\bar{\mathbf{M}}_i^*$ and $\bar{\mathbf{M}}_i$ that are conservative representation of the errors.

## 4. APPLICATION AND DISCUSSION

The POD adjoint-based error measure for mesh optimization has been tested in a 2D gyre flow. The functional to represent the flow dynamics has been defined in terms of the misfit between the POD velocity results and the observational data (case 1) and the vorticity (case 2). The comparison between the results resolved with the original structured mesh and the optimal mesh (adapted to optimize the accuracy of the functional) has been carried out. The root mean square error (RMSE) between the POD velocity solution and the true one at the time level $n$ is used to estimate the error of the POD model:

$$\mathrm{RMSE}^n = \sqrt{\frac{\sum_{i=1}^{\mathscr{N}} (\psi_i^n - \psi_{0,i}^n)^2}{\mathscr{N}}} \tag{42}$$

where $\psi_i^n$ and $\psi_{0,i}^n$ are the POD solution and true one at node $i$, respectively, $\mathscr{N}$ is the total number of nodes over the domain.



DOI: 10.1002/fld

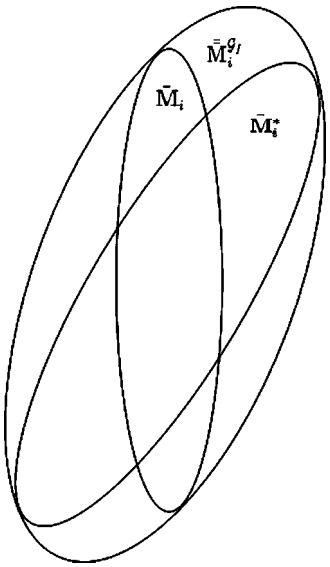


Figure 1. The metric tensors $\bar{\mathbf{M}}_i$ and $\bar{\mathbf{M}}_i^*$.

### *4.1. Description of an ocean gyre test case*

The POD-reduced adjoint model is tested in a computational domain, 1000 km by 1000 km with a depth of $H = 500$ m. The wind forcing on the free surface is given as

$$\tau_y = \tau_0 \cos(\pi y/L), \quad \tau_x = 0.0 \tag{43}$$

where $\tau_x$ and $\tau_y$ are the wind stresses on the free surface along the $x$ and $y$ directions, respectively, and $L = 1000$ km. A maximum zonal wind stress of $\tau_0 = 0.1\,\mathrm{N\,m^{-1}}$ is applied in the latitude ($y$) direction. The Coriolis terms are taken into account with the beta-plane approximation ($f = \beta y$), where $\beta = 1.8 \times 10^{-11}$ and the reference density $\rho_0 = 1000\,\mathrm{kg\,m^{-1}}$.

The problem is nondimensionalized with the maximum Sverdrup balance velocity

$$\beta H \rho_0 v = \frac{\partial \tau}{\partial y} \leqslant \frac{\tau_0 \pi}{L} \Rightarrow v \leqslant 3.5 \times 10^{-2}\,\mathrm{m\,s^{-1}} \tag{44}$$

(and so the velocity scale $U = 3.5 \times 10^{-2}\,\mathrm{m\,s^{-1}}$ is used here). Time is nondimensionalized with $T = L/U$. Incorporating the beta-plane approximation gives a nondimensional $\beta^* = L^2\beta/U = 514.286$. The nondimensional wind stress (applied as a body force here averaged over the depth of the domain) takes the same cosine of latitude profile with $\tau_0^* = \tau_0 L/(U^2 \rho_0 H) = 163.2653$. The Reynolds number is defined as $Re = UL/\nu = 250$ (here the kinematic viscosity is $140\,\mathrm{m^2\,s^{-1}}$). The time step is $3.78 \times 10^{-4}$, equivalent to 3 h. No-slip boundary conditions are applied to the lateral boundaries. The spin-up period is 0.3024 (100 days). The simulation period is [100, 200] days. The initial structured mesh consists of 7442 nodes and 21 600 elements (Figure 2(a)).



DOI: 10.1002/fld

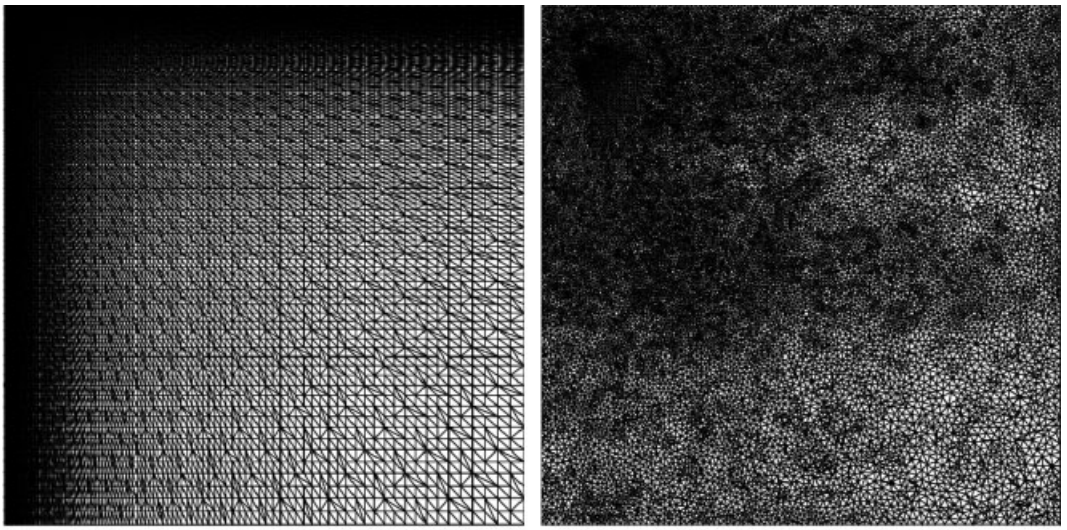


Figure 2. Meshes for the primal and adjoint models. Left panel: the original structured mesh; right panel: the mesh adapted to minimize the misfit between the POD results and exact ones.

### *4.2. Numerical model*

The method outlined in this paper is used in conjunction with the Imperial College Ocean Model (ICOM) [51, 52]. The underlying model equations consist of the 3D incompressible Navier–Stokes equations,

$$\nabla \cdot \mathbf{u} = 0 \tag{45}$$

$$\frac{\partial \mathbf{u}}{\partial t} + \mathbf{u} \cdot \nabla \mathbf{u} + f\mathbf{k} \times \mathbf{u} + \nabla p - \nabla \cdot \boldsymbol{\tau} - s = 0 \tag{46}$$

where $\mathbf{u} \equiv (u, v, w)^{\mathrm{T}} \equiv (u_1, u_2, u_3)^{\mathrm{T}}$ is the velocity vector, $\mathbf{x} \equiv (x, y, z)^{\mathrm{T}} \equiv (x_1, x_2, x_3)^{\mathrm{T}}$ are the orthogonal Cartesian coordinates, $p$ is the perturbation pressure ($p := p/\rho_0$, $\rho_0$ is the constant reference density), $f$ represents the Coriolis inertial force and $s$ is a source term including the wind stress on the free surface and $\mathbf{k} = (0, 0, 1)^{\mathrm{T}}$. The stress tensor $\boldsymbol{\tau}$ is used to represent viscous terms (details in [51]). It is a nonhydrostatic model. The pressure is split into the geostrophic and ageostrophic parts, which are solved for separately. This allows the accurate representation of hydrostatic/geostrophic balance.

The POD-reduced order primal and adjoint models have been developed for ICOM [53]. To accurately represent the geostrophic balance, the POD bases for the geostrophic pressure are split into two sets of POD bases associated with the velocity components $u$ and $v$. The geostrophic pressure has a quadratic finite element representation, while linear finite element representations are used for the velocity components (details in [46]). The calculation of the error measures in (41) (involving the solution of the reduced primal and adjoint models, see (31) and (38)) is carried out in the reduced space, thus significantly reducing the computer cost. The residual in the continuous equations (45) and (46) is ignored in this study.



DOI: 10.1002/fld

### *4.3. Optimized/adaptive meshes using the adjoint-based error measure*

*4.3.1. Case 1*: *Optimized mesh for inversion problems—the optimization of initial conditions.* The aim in this test case is to seek an optimal mesh for an inversion problem, the optimization of the initial conditions. The functional for determining an error measure to guide to adapt the mesh is defined in terms of the misfit between the POD velocity results and the observational data. The functional $f(\psi)$ in (14) is defined here:

$$f(\psi)=\sum_{n=1}^{\mathrm{NT}}\frac{1}{2}\omega^n(\psi^n-\psi_o^n)^{\mathrm{T}}(\psi^n-\psi_o^n) \tag{47}$$

where $\psi_o^n=(u_o^n, v_o^n, w_o^n)^{\mathrm{T}}$ and $\psi^n=(u^n, v^n, w^n)^{\mathrm{T}}$ are the pseudo-observational data (taken at time levels $t_o=112.5$, 125, 137.5, 150, 162.5, 175 and 187.5 days) and the numerical solution from the POD primal model, respectively, $n$ denotes the time index, NT is the number of time levels and $\omega^n$ is the weight that gives a value of 1 at the time level where the pseudo-observational data are available, while 0 at other time levels. The estimated initial conditions are given by the background flow (here, taken from the 'true' flow fields on day 107.5 in the experiments).

The mesh (containing 9914 nodes and 29 175 elements) adapted to minimize the functional in (14) (along with (47)) is shown in Figure 2(b). The optimal mesh is expected to resolve the fields $(u, v, w)$ (the intense boundary current and eddies) at all time levels, to an optimal (with respect to the functional) level of accuracy. The snapshots are recalculated using the optimal mesh and then the POD bases are updated. The POD primal model is driven by the estimated initial conditions and rerun on the optimal mesh.

The results resolved from the POD reduced model using the initial structured mesh and optimal mesh are compared with the true values that are obtained from the full model initialized by the exact initial conditions (i.e. the solution from the full model on day 100). It is shown in Figure 3 that although there is an error (a value of $2.5\,\mathrm{m\,s^{-1}}$) in the estimated initial conditions, by introducing the optimal mesh, the error in the POD results remains small (less than $1.5\,\mathrm{m\,s^{-1}}$ after day 142). Compared with that using the initial structured mesh, the RMSE between the true values and the POD results with the use of the optimal mesh is reduced by half when $t\geqslant 150$ days) while the correlation of velocity results is increased from 75 to 90% (Figure 3). The absolute error between the POD speed results and the true ones over the domain at time levels ($t=100, 150, 175, 200$ days) is shown in Figures 4 and 5. The error between the POD speed results and the true ones decreases by 10–50% in the larger part of flow after introducing the optimal mesh (Figure 5). The velocity fields resolved from the POD model on the optimal mesh are drawn in Figure 6 and exhibit an overall good agreement with the true values (left panel in Figure 6).

Although the calculation of the metric for optimizing the mesh requires additional computations, these costs are offset by applying model-order reduction. Compared with the CPU time (about 30 h) required for running the full model, the CPU time for running the reduced model decreases by a factor of 10 while about 99% of the energy is captured (where 35 POD bases are chosen with 41 snapshots).

Error estimation is a critical issue in reduced-order modelling [54–56]. Here the error estimation for the POD models is carried out using an approach described in [42], where a spectral norm $\|A^l\|_2$ is defined to estimate the spatial error between the full and reduced models. An error bound for the POD model is given by $\sqrt{\lambda_{(M^l+1)}}$ if $M^l$ POD bases are chosen for the variable $l$, where $\lambda_{(M^l+1)}$ is $(M^l+1)$th eigenvalue of $A^lA^{l,\mathrm{T}}$. The error of the POD velocity results is shown in



DOI: 10.1002/fld

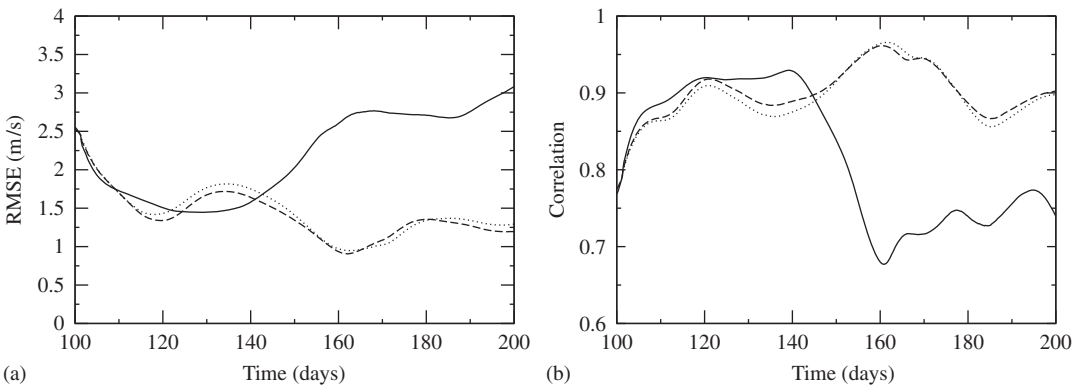


Figure 3. Case 1: (a) RMSE of velocity results and (b) correlation coefficient between the true velocity values and the POD velocity results with the use of the initial structured mesh (solid line) and the mesh adapted to minimize the functional where the observational data are taken either on days 112.5, 125, 137.5, 150, 162.5, 175 and 187.5 (dashed line) or on days 125, 150 and 175 (dotted line). The simulation is driven by the estimated initial condition (the background flow, here, taken from the 'true' flow fields on day 107.5).

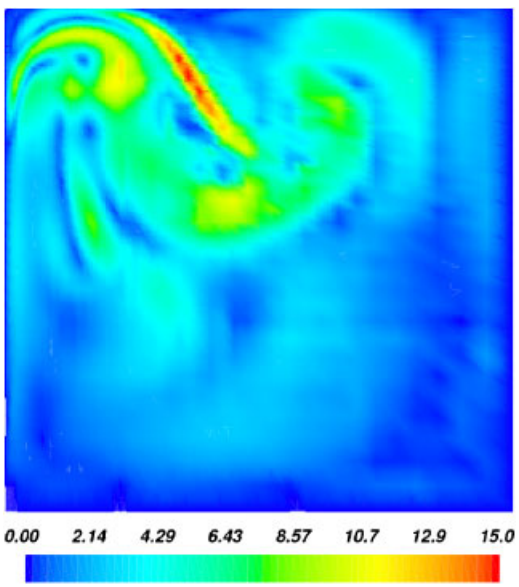


Figure 4. Error in the speed from the POD primal model at the initial time level $t = 100$ days over the computational domain. The error is defined as $\sqrt{(u_i^1 - u_{o,i}^1)^2 + (v_i^1 - v_{o,i}^1)^2}\,(\mathrm{m\,s^{-1}})$, here $u_i^1$ and $v_i^1$ are the estimated initial values at node $i$, and $u_{o,i}^1$ and $v_{o,i}^1$ are the exact initial values at node $i$.



DOI: 10.1002/fld

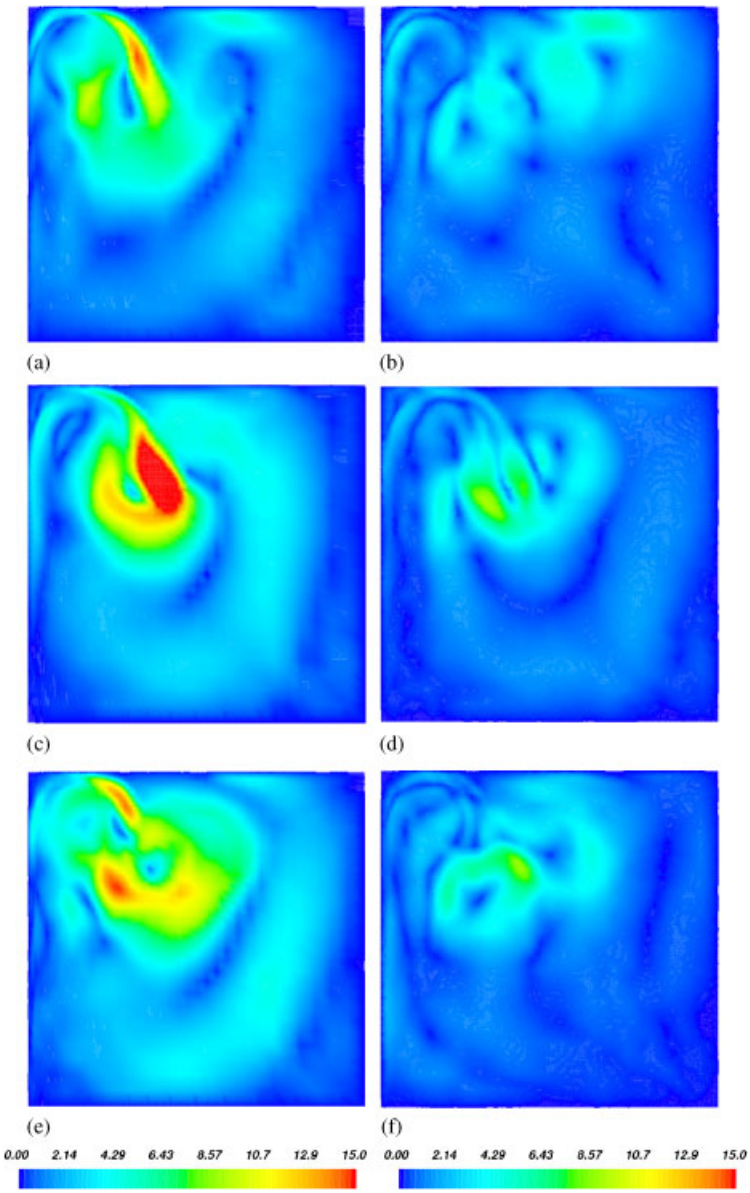


Figure 5. Error in the speed from the POD primal model driven by an estimated initial condition (the background flow, here, taken from the 'true' flow fields on day 107.5) at time levels ($t = 150, 175, 200$ days). Left panel: calculated on the initial structured mesh; right panel: calculated on the mesh adapted to minimise the functional defined as the misfit between the POD results and the observational data. The error is defined as the misfit between the POD solutions ($u_i^n$ and $v_i^n$) and the true values ($u_{o,i}$ and $v_{o,i}$) at node $i$, i.e., $\sqrt{(u_i^n - u_{o,i}^n)^2 + (v_i^n - v_{o,i}^n)^2}$ ($\mathrm{m\,s^{-1}}$), here, $n$ is the time level: (a, b) $t = 100$ days; (c, d) $t = 175$ days; and (e, f) $t = 200$ days.



DOI: 10.1002/fld

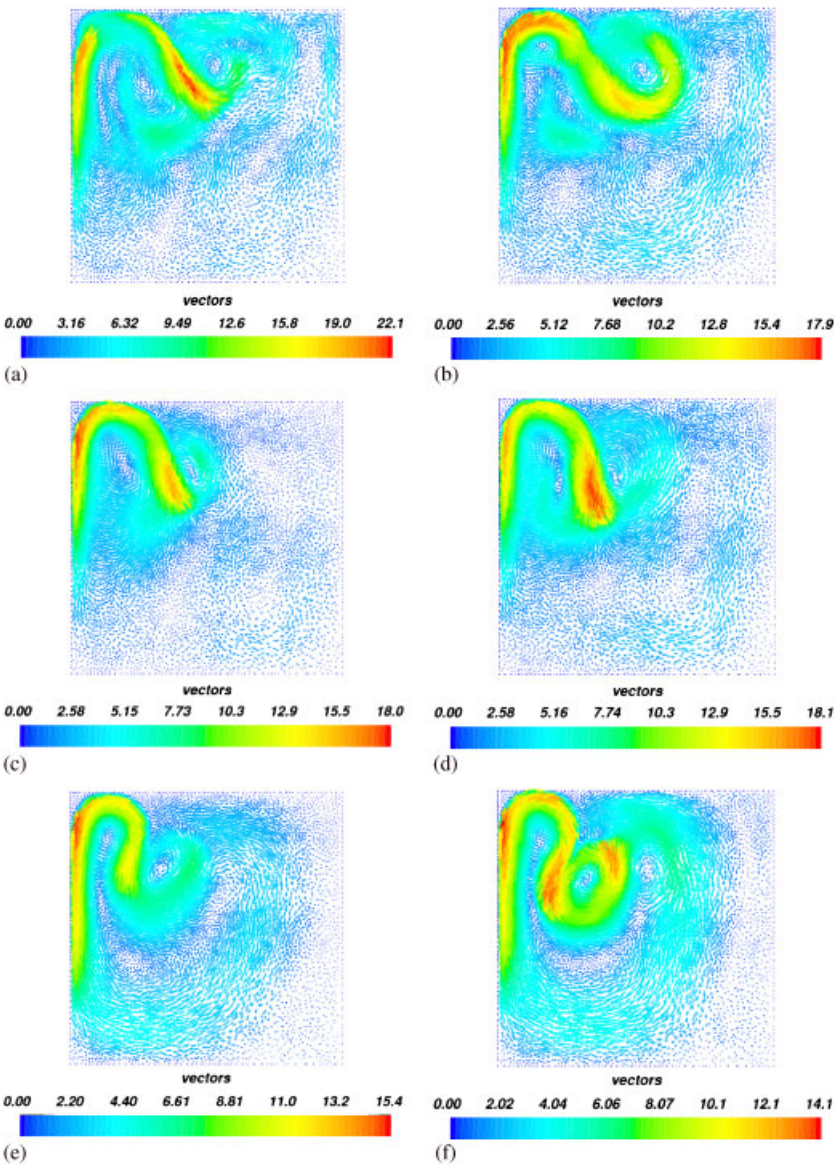


Figure 6. Comparison between the true velocity values and the POD results ($\mathrm{m\,s^{-1}}$). Left panel: the true velocity results obtained from the full model driven by the exact initial condition; right panel: the velocity results from the POD model driven by the estimated initial condition (given by the background flow, here, taken from the 'true' flow fields on day 107.5): (a, b) $t = 100$ days; (c, d) $t = 175$ days; and (e, f) $t = 200$ days.



DOI: 10.1002/fld

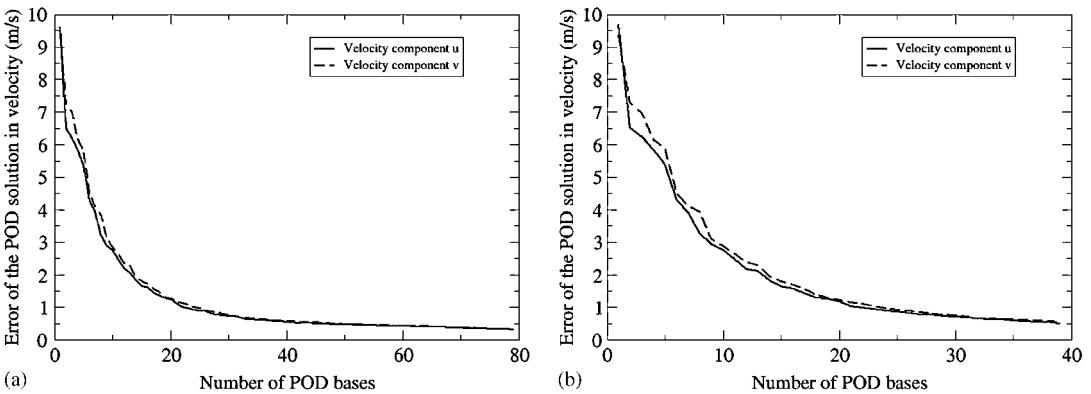


Figure 7. Error of the POD results in $u$ and $v$ ($\|u_{\text{exact}}-u\|_2 \leqslant \sqrt{\lambda_{M^u+1}}$ and $\|v_{\text{exact}}-v\|_2 \leqslant \sqrt{\lambda_{M^v+1}}$). Left panel: 81 snapshots; right panel: 41 snapshots.

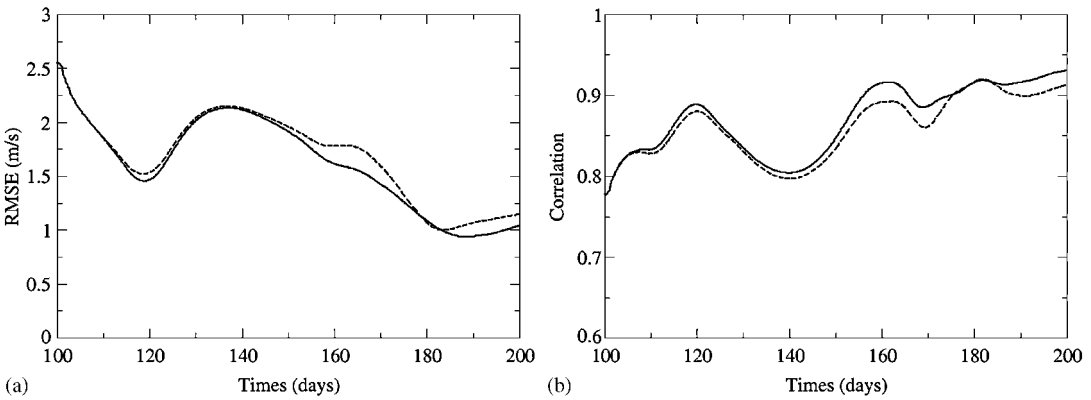


Figure 8. Effect of the number of POD bases on the accuracy of the POD results in case 1 (the solid line: 40 POD bases and the dashed line: 35 POD bases with 41 snapshots): (a) RMSE and (b) correlation coefficient between the true velocity values and the POD velocity results with the use of the mesh adapted to minimize the functional where the observational data are taken either on days 112.5, 125, 137.5, 150, 162.5, 175. The simulation is driven by the estimated initial condition.

Figure 7. It can be seen that the accuracy of the POD model is improved by increasing the number of the POD bases and snapshots. The error of the POD results decreases by 70% of its original values if the first 25% of the leading POD bases are chosen. When a large number of POD bases is taken (here 40 POD bases with either 41 or 81 snapshots), the error of the POD results remains very small (here, less than $0.6\,\text{m}\,\text{s}^{-1}$). Therefore, the POD results are considered to be closer to those from the high-fidelity models (here, almost 100% of energy can be captured when 40 POD bases with 41 snapshots are chosen). The comparison of POD results is provided in Figure 8. It can be seen that compared with that using 35 POD bases, the error in POD results (caused by the estimated initial condition) is reduced by 10% during days 187–200 and 155–170 when 40 POD bases are retained.



DOI: 10.1002/fld

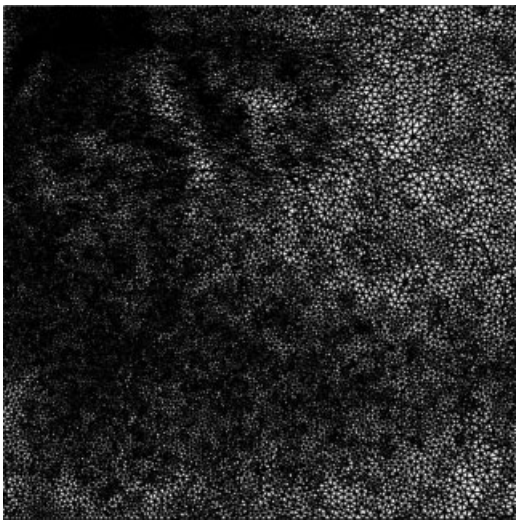

Figure 9. Mesh adapted to optimize the accuracy of the vorticity functional (9858 nodes and 29 362 elements).

*4.3.2. Case 2: Mesh adapted to optimize the accuracy of vorticity.* In this case, the mesh is adapted to maximize the accuracy of the vorticity of the flow dynamics. The functional in (14) is defined as

$$f(\zeta) = \sum_{n=1}^{\mathrm{NT}} \frac{1}{2}(\zeta^n)^2 \tag{48}$$

where $\zeta^n$ is vorticity for 2D flows $\zeta^n = \partial v^n/\partial x - \partial u^n/\partial y$ at time level $n$ and NT is the number of time levels.

The optimal mesh (containing 9858 nodes and 293 62 elements) is drawn in Figure 9. Areas highlighted by both the Hessian of the primal/adjoint solution and the residual during the whole simulation period can be seen to be receiving mesh refinement, while in other areas the mesh is coarsened. Increased mesh resolution is concentrated around the western boundary and the area where the eddies are highly active.

The POD primal model is rerun and driven by the exact initial conditions that are the solutions from the full model on day 100. For comparison, the POD primal model is established and run on both the initial structured mesh and the optimal mesh. The RMSE and correlation coefficient between the POD velocity results and the true values at different time levels are provided in Figure 10. The solid and dashed lines represent the solution with the use of the initial structured mesh and the optimal mesh, respectively. It can be seen that with the use of the initial structured mesh, as the simulated time accrues, the RMSE between the POD results and the true ones increases up to $2\,\mathrm{m\,s^{-1}}$ while the correlation of the velocity results decreases to 84%. By introducing the optimal mesh, the accuracy of the POD results is improved (the RMSE of the velocity results is less than $1\,\mathrm{m\,s^{-1}}$ on day 200, while the correlation coefficient of the velocity results is increased to 92%) during [155, 200] days where the resolution of the optimal mesh can reflect the flow dynamics of highly active eddies. The vorticity results on days 160 and 175 are shown in Figure 11 and exhibit an overall good agreement with exact ones.



DOI: 10.1002/fld

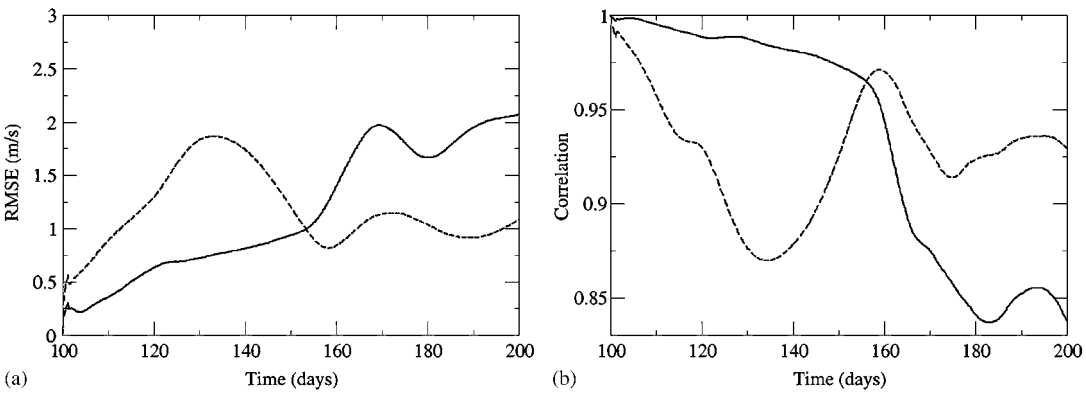


Figure 10. Case 2: (a) RMSE of velocity results and (b) correlation coefficient of velocity results between the full and POD models. The solid line: with the use of the initial structured mesh; the dashed line: with the use of the optimal mesh adapted to maximize the functional defined in (14) along with (48). The simulation is driven by the exact initial condition.

## 5. CONCLUSION

An approach for designing an error measure to guide an adaptive meshing algorithm using a POD adjoint-based or goal-based method is described here. This approach is implemented within the ICOM), a 3D adaptive, nonhydrostatic finite element model. The method employs both primal and adjoint computations to calculate a sensitivity, thereby highlighting locations of the domain that warrant increased or decreased resolution. This is a first attempt to introduce POD into the goal-based error measure for optimizing meshes. The calculation of the goal-based measures is carried out on the reduced space. The reduced-order primal and adjoint models can be run with negligible computational cost as long as a set of sub-matrices for the discretized primal and adjoint models are constructed [46].

The capabilities of the approach, developed here, is demonstrated by a barotropic wind-driven gyre problem. The approach is used to design the error indicators for optimizing the finite element meshes to optimally represent a functional. In the applications presented, this functional is either an integral over space and time of vorticity or the data misfit functional associated with the inverse problem. The former is a representation of the dynamics of the system and the latter functional helps to maximize the accuracy of the inverse problem. Both the velocity and vorticity results from the POD reduced-order model exhibit an overall good agreement with those obtained from the full model. It is also shown that the use of the optimal adaptive mesh leads to an improvement in the correlation coefficient and the reduction in the RMSE between the POD velocity results and the true values.

The POD goal-based error measure algorithm has demonstrated innovative advantages over existing goal-based techniques in its ability: (1) to implement the consistent reduced-order adjoint model from the reduced primal model easily, (2) to significantly reduce the computation cost (here by a factor of 10 in the test cases) of forming the error indicators by carrying out the calculation of the overall adjoint-based error measure (involving in the primal and adjoint solutions) in the



DOI: 10.1002/fld

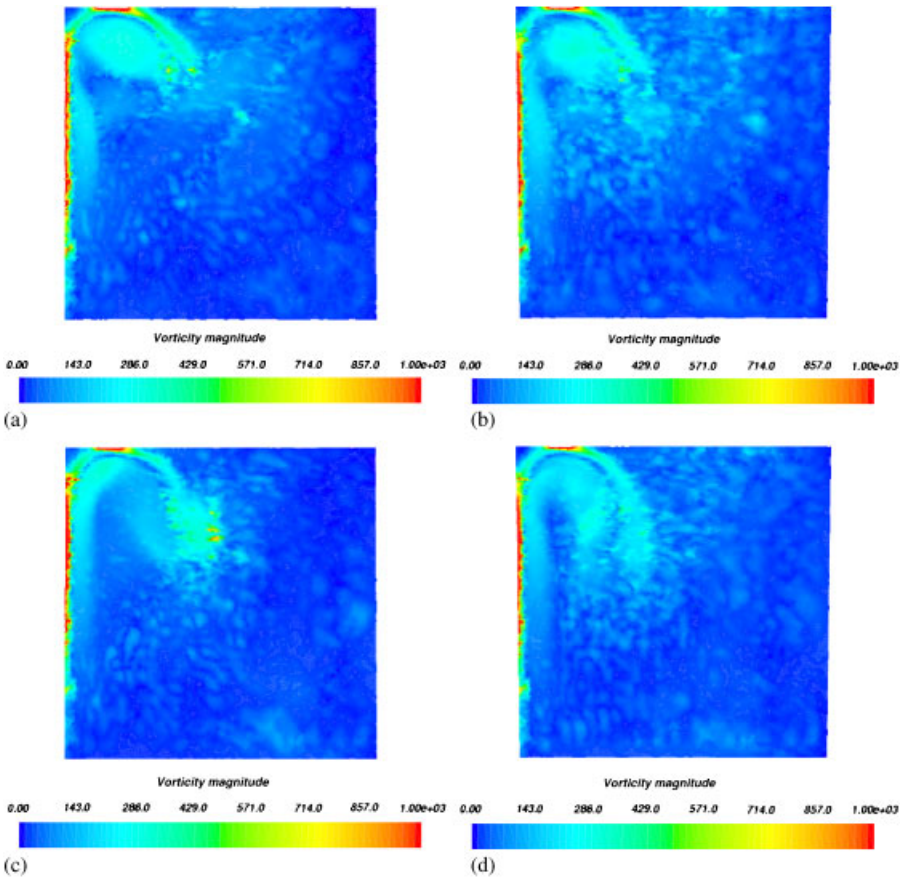


Figure 11. Vorticity at time levels ($t = 160, 175$ days). Left panel: resolved from the full model; right panel: resolved from the POD model with the use of the mesh adapted to minimize the functional defined in (14): (a) $t = 160$ days; (b) $t = 160$ days; (c) $t = 175$ days; and (d) $t = 175$ days.

reduced space. Future work will involve optimizing the dual-weighted POD approach again using goals and applications to 4D Var data assimilation.

ACKNOWLEDGEMENTS

This work was carried out under funding from the U.K.'s Natural Environment Research Council (projects NER/A/S/2003/00595, NE/C52101X/1 and NE/C51829X/1), the Engineering and Physical Sciences Research Council (GR/R60898) and the Leverhulme Trust (F/07058/AB), and with support from the Imperial College High Performance Computing Service and the Grantham Institute for Climate Change. Prof. I. M. Navon would like to acknowledge support of NSF grants ATM-0201808 and CCF-0635162. Finally, the authors would like to thank the two anonymous reviewers who assisted in substantially improving this paper.



DOI: 10.1002/fld

REFERENCES


1. Rannacher R, Suttmeier FT. *A-posteriori* error control in finite element methods via duality techniques: application to perfect plasticity. *Computational Mechanics* 1998; **21**:123–133.
2. Paraschivoiu M, Patera A. A hierarchical duality approach to bounds for the outputs of partial differential equations. *Computer Methods in Applied Mechanics and Engineering* 1998; **158**:389–407.
3. Peraire J, Patera AT. Bounds for linear-functional outputs of coercive partial differential equations: local indicators and adaptive refinement. In *Advances in Adaptive Computational Methods in Mechanics*, Ladevèze P, Oden JT (eds). Elsevier, Oxford, 1998; 199–215.
4. Peraire J, Vahdati M, Morgan K, Zienkiewicz OC. Adaptive remeshing for compressible flow computations. *Journal of Computational Physics* 1987; **72**:449–466.
5. Wu J, Zhu JZ, Szmelter J, Zienkiewicz OC. Error estimation and adaptivity in Navier–Stokes incompressible flows. *Computational Mechanics* 1990; **6**:259–270.
6. Lohner R, Morgan K, Zienkiewicz OC. An adaptive finite element procedure for compressible high speed flows. *Computer Methods in Applied Mechanics and Engineering* 1985; **51**:441–465.
7. Piggott MD, Pain CC, Gorman GJ, Power PW, Goddard AJH. $h, r$ and $hr$ adaptivity with applications in numerical ocean modelling. *Ocean Modelling* 2005; **10**:95–113.
8. Strouboulis T, Oden JT. *A-posteriori* error estimation of finite element approximations in fluid mechanics. *Computer Methods in Applied Mechanics and Engineering* 1990; **78**:201–242.
9. Ainsworth M, Oden JT. *A-posteriori* error estimation in finite element analysis. *Computer Methods in Applied Mechanics and Engineering* 1997; **142**:1–88.
10. Ainsworth M, Oden JT. A unified approach to *a-posteriori* error estimation using element residual methods. *Numerische Mathematik* 1993; **65**:23–50.
11. Babuska I, Rheinboldt WC. *A-posteriori* error estimates for the finite element method. *International Journal for Numerical Methods in Engineering* 1978; **12**:1597–1615.
12. Bank RE, Smith RK. *A-posteriori* error estimates based on hierarchical bases. *SIAM Journal on Mathematical Analysis* 1993; **30**:921–935.
13. Bank RE, Weiser A. Some *a-posteriori* error estimators for elliptic partial differential equations. *Mathematics of Computation* 1985; **44**:283–301.
14. Verfurth R. *A Review of a-posteriori Error Estimation and Adaptive Mesh-refinement Techniques*. Wiley, Teubner: Chichester, Stuttgart, 1996.
15. Zienkiewicz OC, Zhu JZ. The superconvergent patch recovery and *a-posteriori* error estimates. Part 1: the recovery technique. *International Journal for Numerical Methods in Engineering* 1992; **33**:1331–1364.
16. Zienkiewicz OC, Zhu JZ. The superconvergent patch recovery and *a-posteriori* error estimates. Part 2: error estimates and adaptivity. *International Journal for Numerical Methods in Engineering* 1992; **33**:1365–1382.
17. Pierce NA, Giles MB. Adjoint recovery of superconvergent functionals from PDE approximations. *SIAM Review* 2000; **42**:247–264.
18. Oden JT, Prudhomme S. Goal-oriented error estimation and adaptivity for the finite element method. *Computers and Mathematical Applications* 2001; **41**:735–756.
19. Prudhomme S, Oden JT. On goal-oriented error estimation for elliptic problems. *Computer Methods in Applied Mechanics and Engineering* 1999; **179**:313–331.
20. Cirak F, Ramm E. *A-posteriori* error estimation and adaptivity for linear elasticity using the reciprocal theorem. *Computer Methods in Applied Mechanics and Engineering* 1998; **156**:351–362.
21. Venditti DA, Darmofal DL. Adjoint error estimation and grid adaptation for functional outputs: application to quasi-one-dimensional flow. *Journal of Computational Physics* 2000; **164**:204.
22. Venditti DA, Darmofal DL. Grid adaptation for functional outputs: application to two-dimensional inviscid flows. *Journal of Computational Physics* 2002; **176**:40–69.
23. Venditti DA, Darmofal DL. Anisotropic grid adaptation for functional outputs: application to two-dimensional viscous flows. *Journal of Computational Physics* 2003; **187**:22–46.
24. Balasubramanian R. Error estimation and grid adaptation for functional outputs using discrete adjoint sensitivity analysis. *Master Thesis*, Mississippi State University, December 2002.
25. Müller J-D, Giles MB. Solution adaptive mesh refinement using adjoint error analysis. *Fifteenth Computational Fluid Dynamics Conference*, American Institute of Aeronautics and Astronautics, June 2001.
26. Park MA. Adjoint-based, three-dimensional error prediction and grid adaptation. *AIAA Paper 2002-3286*, 2002.
27. Park MA. Three-dimensional turbulent RANS adjoint-based error correction. *AIAA Paper, 2003-3849*, 2002.




DOI: 10.1002/fld

28. Micheletti S, Formaggia L, Perotto S. Anisotropic mesh adaptation in computational fluid dynamics: application to the advection–diffusion–reaction and the Stokes problems. *Applied Numerical Mathematics* 2004; **51**:511–533.
29. Power PW, Pain CC, Piggott MD, Gorman GJ, Fang F, Marshall DP, Goddard AJH. Adjoint goal-based error norms for adaptive mesh ocean modelling. *Ocean Modelling* 2006; **15**:3–38. DOI: 10.1016/j.ocemod.2006.05.001.
30. Nielsen EJ, Lu J, Park MA, Darmofal DL. An implicit, exact dual adjoint solution method for turbulent flows on unstructured grids. *Computers and Fluids* 2004; **33**:1131–1155.
31. Willcox K, Peraire J. Balanced model reduction via the proper orthogonal decomposition. *AIAA Journal* 2002; **40**(11):2323–2330.
32. Willcox K, Ghattas O, van Bloemen Waanders B, Bader B. An optimization framework for goal-oriented, model-based reduction of large-scale systems. *IEEE Conference on Decision and Control and European Control Conference* (CDC–ECC), Seville, Spain, 12–15 December 2005.
33. Bui-Thanh T, Willcox K, Ghattas O, van Bloemen Waanders B. Goal-oriented, model-constrained optimization for reduction of large-scale systems. *Journal of Computational Physics* 2007; **224**(2):880–896.
34. Daescu DN, Navon IM. A dual-weighted approach to order reduction in 4d-var data assimilation. *Monthly Weather Review* 2008; **136**(3):1026–1041.
35. Meyer M, Matthies HG. Efficient model reduction in non-linear dynamics using the Karhunen–Loeve expansion and dual-weighted-residual methods. *Computional Mechanics* 2003; **17**(1–4):179–191.
36. Kunish K, Volkwein S. Galerkin proper orthogonal decomposition methods for a general equation in fluid dynamics. *SIAM Journal on Numerical Analysis* 2002; **40**(2):492–515.
37. Aubry N, Holmes P, Lumley JL. The dynamics of coherent structures in the wall region of a turbulent boundary layer. *Journal of Fluid Dynamics* 1988; **192**:115–173.
38. Everson R, Sirovich L. Karhunen–Loève procedure for gappy data. *Journal of the Optical Society of America A* 1995; **12**:1657–1664.
39. Homescu C, Petzold LR, Serban R. Error estimation for reduced-order models of dynamical systems. *SIAM Review* 2007; **49**(2):277–299.
40. Hoteit I, Kohl A. Efficiency of reduced-order, time-dependent adjoint data assimilation approaches. *Journal of Oceanography* 2006; **62**(4):539–550.
41. Iollo A, Lanteri S, Desideri JA. Stability properties of POD-Galerkin approximations for the compressible Navier–Stokes equations. *Theoretical and Computational Fluid Dynamics* 2000; **13**:377–396.
42. Luo Z, Chen J, Zhu J, Wang R, Navon IM. An optimizing reduced order FDS for the tropical Pacific ocean reduced gravity model. *International Journal for Numerical Methods in Fluids* 2007; **55**:143–161.
43. Luo Z, Zhu J, Wang R, Navon IM. Proper orthogonal decomposition approach and error estimation of mixed finite element methods for the tropical Pacific ocean reduced gravity model. *Computer Methods in Applied Mechanics and Engineering* 2007; **196/41–44**:4184–4195.
44. Ravindran SS. Adaptive reduced-order controllers for a thermal flow system using proper orthogonal decomposition. *SIAM Journal on Scientific Computing* 2002; **23**(6):1924–1942.
45. Cao Y, Zhu J, Navon IM, Luo Z. A reduced order approach to four-dimensional variational data assimilation using proper orthogonal decomposition. *International Journal for Numerical Methods in Fluids* 2006; **53**(10):1571–1583.
46. Fang F, Pain CC, Navon IM, Piggott MD, Gorman GJ, Goddard AJH. Reduced order modelling of an adaptive mesh ocean model. *International Journal for Numerical Methods in Fluids* 2009; **59**(8):827–851.
47. Robert C, Durbiano S, Blayo E, Verron J, Blum J, le Dimet FX. A reduced-order strategy for 4D-VAR data assimilation. *Journal of Marine Systems* 2005; **57**(1–2):70–82.
48. Sirovich L, Kirby M. Low-dimensional procedure for the characterization of human faces. *Journal of the Optical Society of America A* 1987; **4**(3):519–524.
49. Hinze M, Volkwein S. Proper orthogonal decomposition surrogate models for nonlinear dynamical systems: error estimates and suboptimal control. In *Dimension Reduction of Large-scale Systems*, Benner P, Mehrmann V, Sorensen D (eds). Lecture Notes in Computational and Applied Mathematics. 2005; 261–306.
50. Pain CC, Umpleby AP, de Oliveira CRE, Goddard AJH. Tetrahedral mesh optimisation and adaptivity for steady-state and transient finite element calculations. *Computer Methods in Applied Mechanics and Engineering* 2001; **190**:3771–3796.
51. Ford R, Pain CC, Piggott MD, Goddard AJH, de Oliveira CRE, Umbleby AP. A nonhydrostatic finite-element model for three-dimensional stratified oceanic flows. Part I: model formulation. *Monthly Weather Review* 2004; **132**(12):2816–2831.
52. Pain CC, Piggott MD, Goddard AJH, Fang F, Gorman GJ, Marshall DP, Eaton MD, Power PW, de Oliveira CRE. Three-dimensional unstructured mesh ocean modelling. *Ocean Modelling* 2005; **10**(1–2):5–33.

53. Fang F, Pain CC, Navon IM, Piggott MD, Gorman GJ, Farrell PE, Allison P, Goddard AJH. A POD reduced-order 4D-Var adaptive mesh ocean modelling approach. *International Journal for Numerical Methods in Fluids* 2009; **60**(7):709–732.
54. Utku S, Clemente J, Salama M. Errors in reduction methods. *Computers and Structures* 1985; **21**(6):1153–1157.
55. Homescu C, Petzold LR, Serban R. Error estimation for reduced-order models of dynamical systems. *SIAM Journal on Numerical Analysis* 2005; **43**:1693–1714.
56. LeGresley PA, Alonso JJ. Dynamic domain decomposition and error correction for reduced order models. *Forty-first AIAA Aerospace Sciences Meeting and Exhibit*, Reno, NV, *AIAA Paper 2003-0250*, 6–9 January 2003.



DOI: 10.1002/fld